

laxed GB configuration (GB2), B reduces the magnetic moment of Fe(1), Fe(2), and Fe(3) by $0.45 \mu_B$, $0.01 \mu_B$, and $0.17 \mu_B$, respectively. The reduction of the Fe(3) magnetic moment in B-Fe(111), $0.65 \mu_B$, is even a little larger than that in P-Fe(111). The reduction of the Fe magnetization affects the segregation energy (Table 1, see the difference between results of ΔE for ferromagnetic and nonmagnetic states).

Finally, the calculated results for the $\Delta E_b - \Delta E_s$ difference controlling embrittlement are listed in Table 1. Because the impurity-induced structural relaxation is included, the segregation energy for P in the GB environment is smaller (less negative) than that on the FS; that is, $\Delta E_b - \Delta E_s = 0.79 \text{ eV} > 0$, in good agreement with experiment ($0.4 \pm 0.2 \text{ eV}$ per cell). According to the Rice-Wang thermodynamic theory (1), P is thus an embrittler for the Fe Σ 3[110] (111) GB. By contrast, $\Delta E_b - \Delta E_s$ is almost zero (negative for the nonmagnetic case) for B, and thus, B is weakly cohesion enhancing.

Many factors affect the final results of $\Delta E_b - \Delta E_s$. The mechanical energy is especially important because the segregation energy differences are negative for both P and B when relaxation for the clean Fe GB is neglected. The magnetic energies are not large for either ΔE_b or ΔE_s separately (Table 1) but are indeed important for their difference. Therefore, a highly precise spin-polarized method and, importantly, equal treatment for the FS and GB systems are essential to obtain correct predictive results. The net magnetic contributions to the $\Delta E_b - \Delta E_s$ differences (Table 1) show that while magnetism reduces the embrittlement potency of P, it also reduces the cohesion enhancing effect of B.

As discussed earlier, impurity-induced reduction of Fe-Fe bonding is here eliminated as the mechanism for GB embrittlement by the comparison of P and B. Because the embrittlement behavior of an impurity is determined by $\Delta E_b - \Delta E_s$, it is essential to compare the difference of effects in the FS and GB systems. In both the Fe Σ 3[110] (111) GB and the Fe(111) FS, there are three Fe(1) atoms. The strength of impurity-Fe(1) bonding (Fig. 2) does not change greatly from the GB to FS environments and thus is not significant for $\Delta E_b - \Delta E_s$. By contrast, impurity-Fe(3) bonding is expected to play the important role because one out of two of the vertical bonds in the GB is broken in the FS. Therefore, the spatial anisotropy of the bonding interaction between the impurity states with the surrounding Fe atom can be crucial to embrittlement behavior. Simply, impurities with stronger vertical and weaker lateral bonding are favorable to enhance the GB cohesion.

This conclusion is supported by the comparison of P and B. The B-Fe(3) bonding is much stronger than the

B-Fe(1) bonding (bottom panels, Fig. 2); there is even a dangling bond above the B atom for B-Fe(111). Therefore, B prefers the GB environment to saturate the B-Fe(3) bonding. By contrast, P-Fe bonding is more embedded-like (electrostatic), and thus, there is no such dangling bond above P for P-Fe(111) (left top, Fig. 2). In addition, the P-Fe(1) bonding is almost as strong as that of P-Fe(3) bonding. Only one out of five P-Fe bonds in the GB is broken in the FS for P (one out of two for B), and thus, the reduction of the chemical energy for P is smaller than that for B. This is the main reason why the chemical part of $\Delta E_b - \Delta E_s$ for B is two times larger than that for P. Calculations for C and S impurities are in progress to verify the generality of these bonding trends, and further calculations will explore the interactions of impurity segregants and alloying elements. The fundamental insights developing from this research hold promise for new directions in alloy composition for enhancement of GB-sensitive properties.

REFERENCES AND NOTES

1. J. R. Rice and J.-S. Wang, *Mater. Sci. Eng. A* 107, 23 (1989).
2. P. M. Anderson, J.-S. Wang, J. R. Rice, in *Innovations in Ultrahigh-Strength Steel Technology*, G. B.

- Olson, M. Azrin, E. S. Wright, Eds. (Proceedings of the 34th Sagamore Army Materials Research Conference, Government Printing Office, Washington, DC, 1990), p. 619.
3. G. B. Olson, *ibid.*, pp. 3-66.
4. In this notation, Σ 3 refers to a special orientation relation between crystals for which one in three lattice points are coincident, [110] denotes the crystal Miller indices of the axis of misorientation, and (111) denotes the habit plane of the boundary, both referred to the body-centered-cubic crystal lattice of Fe.
5. R.-q. Wu, A. J. Freeman, G. B. Olson, *J. Mater. Res.* 7, 2403 (1992).
6. ———, *Phys. Rev. B*, in press.
7. S. P. Tang, A. J. Freeman, G. B. Olson, *ibid.* 47, 2441 (1993).
8. R.-q. Wu, A. J. Freeman, G. B. Olson, *ibid.*, p. 6855.
9. G. L. Krasko and G. B. Olson, *Solid State Commun.* 76, 247 (1990).
10. R.-q. Wu and A. J. Freeman, *Phys. Rev. B* 47, 3904 (1993).
11. G. L. Krasko, in *Structure and Properties of Interfaces in Materials*, W. A. T. Clark, U. Dahmen, C. L. Briant, Eds. (MRS Symp. Proc. 238, Materials Research Society, Pittsburgh, PA, 1991), pp. 481.
12. R.-q. Wu and A. J. Freeman, *Comput. Phys. Commun.* 76, 58 (1993).
13. C. L. Briant and R. P. Messmer, *Philos. Mag. B* 42, 569 (1980).
14. Supported by the Office of Naval Research (grant N00014-90-J-1363) with seed funding from the National Science Foundation (NSF) Materials Research Laboratory program (grant DMR88-16126) and a grant of Cray-C90 computer time at the NSF Pittsburgh Supercomputing Center from its Division of Advanced Scientific Computing.

8 February 1994; accepted 20 May 1994

Synthesis and Properties of a Cuprate Superconductor Containing Double Mercury-Oxygen Layers

P. G. Radaelli, M. Marezio, M. Perroux, S. de Brion, J. L. Tholence, Q. Huang, A. Santoro

A cuprate superconductor containing double mercury layers was synthesized with a high-pressure, high-temperature technique. The compound, with chemical formula $\text{Hg}_2\text{Ba}_2\text{Y}_{1-x}\text{Ca}_x\text{Cu}_2\text{O}_{8-8}$, contains a double HgO layer with structure similar to that of rock salt. The prototype compound $\text{Hg}_2\text{Ba}_2\text{YCu}_2\text{O}_{8-8}$ is an insulator. Superconductivity is induced in the system by partially replacing yttrium with calcium.

All known copper-based superconductors have layered structures, where CuO_2 planes alternate with other structural elements. The compounds with the highest superconducting critical temperatures all contain,

P. G. Radaelli and M. Perroux, Laboratoire de Cristallographie, CNRS/UJF, BP 166, 38042 Grenoble Cedex 09, France.

M. Marezio, Laboratoire de Cristallographie, CNRS/UJF, BP 166, 38042 Grenoble Cedex 09, France, and AT&T Bell Laboratories, Murray Hill, NJ 07974, USA.

S. de Brion and J. L. Tholence, Centre de Recherche sur les Très Basses Températures, CNRS/UJF, BP 166, 38042 Grenoble Cedex 09, France.

Q. Huang and A. Santoro, National Institute of Standards and Technology, Reactor Division, Gaithersburg, MD 20899, USA.

besides one or more CuO_2 planes; a single or double heavy metal-oxygen layer, like BiO , TlO , or HgO_8 . In the case of bismuth-based compounds, only structures containing double bismuth-oxygen layers have been synthesized (1). Thallium-containing superconductors can be formed with both a single and a double TlO layer (2, 3). In 1993, a series of superconducting cuprates containing mercury was discovered. These compounds contain a single HgO_8 layer, where mercury is bonded with two oxygen atoms along the z axis, as in a dumbbell (4). However, double mercury layers are occasionally observed by electron imaging as

defects in a single-mercury-layer matrix.

We synthesized a cuprate superconductor containing double mercury-oxygen layers. The compound, with chemical formula $\text{Hg}_2\text{Ba}_2\text{Y}_{1-x}\text{Ca}_x\text{Cu}_2\text{O}_{8-\delta}$, contains a rock salt-type double HgO layer. The prototype compound $\text{Hg}_2\text{Ba}_2\text{YCu}_2\text{O}_{8-\delta}$, is an insulator. Superconductivity, with a maximum critical temperature of about 45 K, is induced by partially replacing yttrium with calcium.

Samples with nominal composition $\text{Hg}_2\text{Ba}_2\text{YCu}_2\text{O}_{8-\delta}$ and $\text{Hg}_2\text{Ba}_2\text{Y}_{1-x}\text{Ca}_x\text{Cu}_2\text{O}_{8-\delta}$ ($x = 0.3, 0.4, 0.5, 0.7,$ and 1.0) were synthesized at a temperature and pressure of 1000°C and 18 kbar with a belt press apparatus. The starting material was prepared by adding HgO to a precursor consisting of a mixed oxide of the other cations, obtained by vacuum decomposition of the corresponding nitrates. The BaCO_3 , Y_2O_3 , CaCO_3 , and CuO were dissolved in diluted nitric acid. The solution was slowly evaporated, and the dry product was ground and subsequently heated under vacuum up to 800°C . After about 12 hours, oxygen was introduced. After four additional hours, the sample was rapidly quenched to room temperature. To explore the effect of reducing the formal valence of copper, we synthesized another sample with nominal composition $\text{Hg}_{1.7}\text{Pr}_{0.3}\text{Ba}_2\text{YCu}_2\text{O}_{8-\delta}$ by the same technique.

The x-ray powder diffraction data were obtained with a Guinier-Hägg focusing camera with $\text{FeK}\alpha$ radiation (1.93730 \AA). Finely ground silicon ($a = 5.43088 \text{ \AA}$ at 25°C) was used as an internal standard. We collected neutron powder diffraction data at room temperature on three samples, with compositions

$\text{Hg}_2\text{Ba}_2\text{YCu}_2\text{O}_{8-\delta}$, $\text{Hg}_2\text{Ba}_2\text{Y}_{0.6}\text{Ca}_{0.4}\text{Cu}_2\text{O}_{8-\delta}$, and $\text{Hg}_{1.7}\text{Pr}_{0.3}\text{Ba}_2\text{YCu}_2\text{O}_{8-\delta}$, using a 32-counter diffractometer at the reactor of the National Institute of Standards and Technology. Structural parameters were refined with the GSAS program by Larson and von Dreele (5). Electrical resistivity was measured with a standard dc four-probe apparatus using a current of $2 \times 10^{-6} \text{ A}$. Magnetic susceptibility was measured with an ac susceptometer that used a 0.02-Oe measuring field.

The x-ray pattern of the $x = 0$ sample is shown in Fig. 1A. All the Bragg peaks can be indexed on a body-centered tetragonal unit cell of lattice constants $a = 3.875 \text{ \AA}$ and $c = 28.89 \text{ \AA}$; the extinction rules are characteristic of the space group $I4/mmm$. No impurity peaks are present in the diffraction pattern, which has a sensitivity of a few percent. The lattice parameters of $\text{Hg}_2\text{Ba}_2\text{YCu}_2\text{O}_{8-\delta}$ indicate that this compound is quasi-isostructural to the well-known Tl- and Bi-based compounds $\text{Tl}_2\text{Ba}_2\text{CaCu}_2\text{O}_8$ and $\text{Bi}_2\text{Sr}_2\text{CaCu}_2\text{O}_8$. In particular, the body-centering of the tetragonal unit cell is characteristic of the presence of a double "rock salt" metallic layer. If the oxygen site O3 on the HgO layer were fully occupied, each mercury atom in $\text{Hg}_2\text{Ba}_2\text{YCu}_2\text{O}_{8-\delta}$ would be at the center of an apically compressed O_6 octahedron, as in HgO (Fig. 2). The sample had a high electrical resistivity and was not superconducting.

The formal valence of copper in this compound can be both reduced and increased by replacing mercury with praseodymium or by replacing yttrium with calcium, respectively. Like the undoped compound, the Pr-doped sample is nearly single phase according to the

x-ray analysis and is an insulator. When yttrium is replaced by calcium up to a composition of $x = 0.5$, traces of HgCaO_2 (and also CuO , for the $x = 0.5$ sample only) appear as impurity phases (Fig. 1B). However, no traces of known superconducting compounds (like those containing one layer of mercury or members of the

Fig. 1. The x-ray powder diffraction pattern for (A) $\text{Hg}_2\text{Ba}_2\text{YCu}_2\text{O}_{8-\delta}$ and (B) $\text{Hg}_2\text{Ba}_2\text{Y}_{0.6}\text{Ca}_{0.4}\text{Cu}_2\text{O}_{8-\delta}$. The Bragg peaks of the two-mercury-layer phase are indexed on a tetragonal unit cell (space group, $I4/mmm$) with $a \approx 3.87 \text{ \AA}$ and $c \approx 28.9 \text{ \AA}$. The Bragg peaks of silicon (used as internal standard) are marked with an asterisk. In (B), the dots mark the positions of the main peaks of HgCaO_2 , and the arrows indicate the expected positions of the highest peaks of $\text{HgBa}_2\text{CuO}_{4+\delta}$ (at 37.6°) and $\text{HgBa}_2\text{CaCu}_2\text{O}_{6+\delta}$ (at 34.2°).

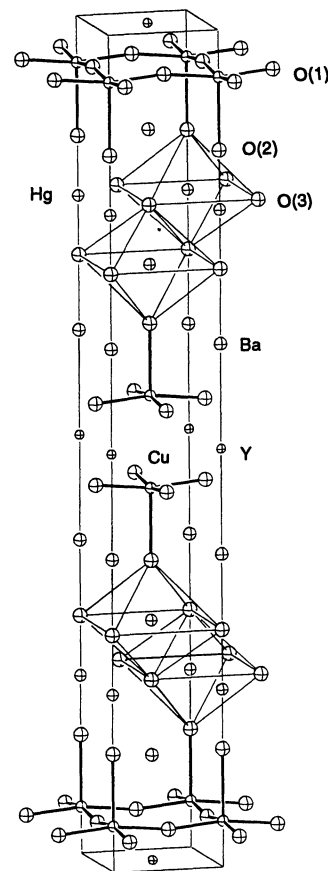
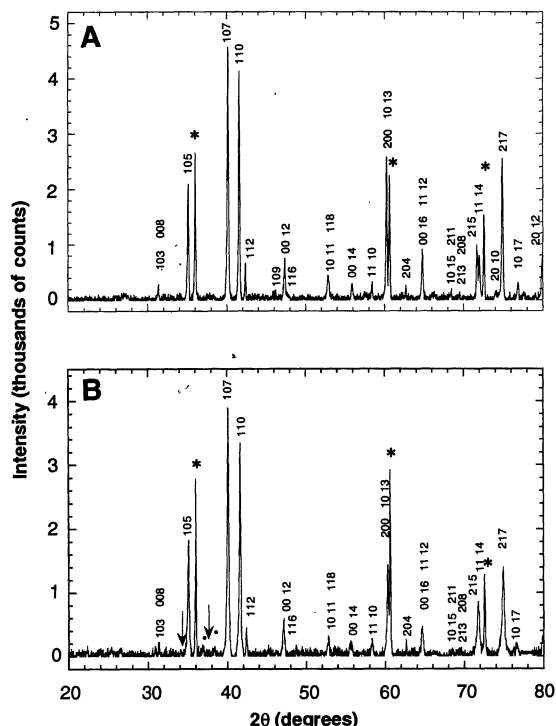


Fig. 2. Crystal structure of $\text{Hg}_2\text{Ba}_2\text{YCu}_2\text{O}_{8-\delta}$. The drawing evidences the edge-sharing octahedral coordination of mercury with oxygen. Oxygen vacancies on the HgO plane are not considered in the drawing.

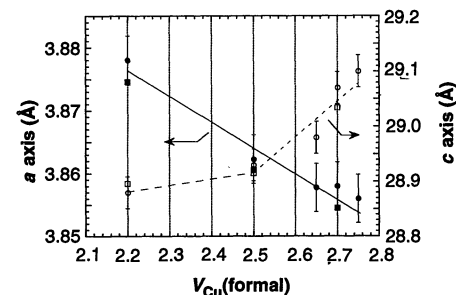


Fig. 3. The a (open symbols) and c (filled symbols) lattice parameters as a function of formal copper valence V_{Cu} for undoped, Pr-doped, and Ca-doped $\text{Hg}_2\text{Ba}_2\text{YCu}_2\text{O}_{8-\delta}$. Circles and squares indicate x-ray and neutron diffraction data, respectively. We calculated V_{Cu} assuming $\delta = 0$ and $V_{\text{Pr}} = +4$. The lines are guides for the eye.

Table 1. Refined structural parameters from neutron powder diffraction data for the $\text{Hg}_2\text{Ba}_2\text{YCu}_2\text{O}_{8-x}$ sample. The space group is $I4/mmm$ (no. 139). Numbers in parentheses are statistical errors of the last significant digit (when absent, the parameter was held fixed). The occupancies n were normalized to one unit formula by multiplying the fractional site occupancy by half of the site multiplicity. $a = 3.8606(1)$ Å; $c = 28.915(1)$ Å; $R_p = 3.97\%$; $R_{wp} = 4.99\%$; $\chi^2 = 1.070$.

Atom	Site	x	y	z	B (Å ²)	n
Y	2b 4/mmm	0.5	0.5	0	0.3(1)	1
Ba	4e 4mm	0.5	0.5	0.1252(2)	0.5(1)	2
Hg	4e 4mm	0	0	0.2126(1)	1.46(6)	2
Cu	4e 4mm	0	0	0.0560(1)	0.30(6)	2
O1	8g 2mmm	0.5	0	0.0495(1)	0.62(6)	4
O2	4e 4mm	0	0	0.1414(3)	1.5(1)	2
O3	16m m	0.574(2)	0.574(2)	0.2163(4)	0.7(4)	1.55(6)

“1-2-3” family) can be detected.

For $x > 0.5$, the lattice parameters cease to vary, indicating that the solubility limit of calcium in the compound has been reached. Under the thermodynamic conditions that we used, the two-mercury-layer phase is not stable without yttrium, and no trace of it can be detected in the $x = 1.0$ sample.

Figure 3 shows the behavior of the lattice constants as a function of the formal copper valence, assuming that the valence state of praseodymium is +4 and that no oxygen vacancies are present throughout the range. The decrease of the a lattice parameter as a function of hole doping is typical of all layered cuprates and is attributable to the removal of electrons from antibonding $\text{Cu}3d\text{-O}2p$ orbitals. However, the slope of the a versus doping curve (~ 0.045 Å per hole) is much lower than that for other cuprates, for which 0.1 Å per hole is a typical value. This observation, along with the overall high values of the formal copper valence, suggests that a mechanism that compensates for the cation doping may be present in this case. The behavior of the c parameter is more consistent with a steric effect: The increase is more pronounced for the calcium-doped samples because of the larger ionic radius of calcium with respect to yttrium.

Rietveld refinements of the structural parameters from neutron diffraction data confirm the general features of the structure of

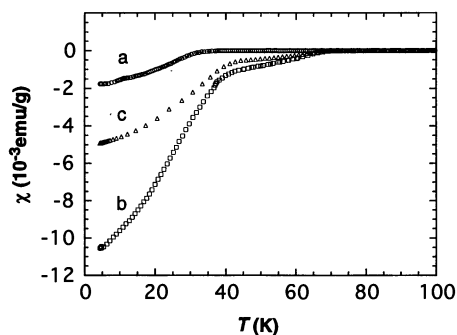


Fig. 4. Susceptibility versus temperature for $\text{Hg}_2\text{Ba}_2\text{Y}_{0.7}\text{Ca}_{0.3}\text{Cu}_2\text{O}_{8-x}$ (curve a), $\text{Hg}_2\text{Ba}_2\text{Y}_{0.6}\text{Ca}_{0.4}\text{Cu}_2\text{O}_{8-x}$ (curve b), and $\text{Hg}_2\text{Ba}_2\text{Y}_{0.5}\text{Ca}_{0.5}\text{Cu}_2\text{O}_{8-x}$ (curve c).

these compounds but reveal important differences with respect to the Bi- and Tl-based “2212” compounds. In particular, the oxygen site O3 is essentially full for the Pr-doped sample, while it accommodates 20 to 25% of vacancies for the $\text{Hg}_2\text{Ba}_2\text{YCu}_2\text{O}_{8-x}$ and $\text{Hg}_2\text{Ba}_2\text{Y}_{0.6}\text{Ca}_{0.4}\text{Cu}_2\text{O}_{8-x}$ samples. This buildup of oxygen vacancies partially compensates for the cation doping, therefore reducing the valence of copper to values between 2.0 and 2.4, which are typical for cuprate superconductors. In addition, O3 is no longer in the high-symmetry position $\frac{1}{2}, \frac{1}{2}, z$ but is displaced up to 0.5 Å toward the mercury atoms. As a consequence of the formation of vacancies on the O3 site, some of the mercury atoms lose one of the neighboring oxygen atoms along the z axis. Therefore, they are no longer at the center of an apically compressed octahedron but acquire a pyramidal coordination, with only one short Hg–O bond along the z axis and three or four in-plane bonds. The displacement of the O3 site results in the formation of stronger in-plane Hg–O bonds as short as 2.33 Å, probably around these mercury atoms. This pyramidal coordination, to the best of our knowledge is novel for mercury in oxides. The structural parameters of the prototype compound $\text{Hg}_2\text{Ba}_2\text{YCu}_2\text{O}_{8-x}$ are reported in Table 1. Selected interatomic

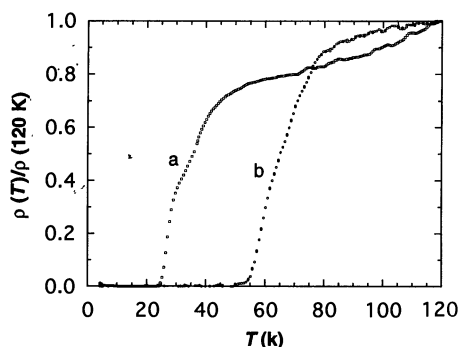


Fig. 5. Resistivity versus temperature for $\text{Hg}_2\text{Ba}_2\text{Y}_{0.7}\text{Ca}_{0.3}\text{Cu}_2\text{O}_{8-x}$ (curve a) and $\text{Hg}_2\text{Ba}_2\text{Y}_{0.6}\text{Ca}_{0.4}\text{Cu}_2\text{O}_{8-x}$ (curve b), normalized to the values at 120 K. The absolute values of the resistivities at 120 K are 1.04×10^{-3} and 1.40×10^{-6} ohm-m for the $x = 0.3$ and 0.4 samples, respectively.

Table 2. Selected interatomic distances for $\text{Hg}_2\text{Ba}_2\text{YCu}_2\text{O}_{8-x}$, as obtained from Rietveld refinement of neutron diffraction data. The parentheses contain the statistical error in the last digit.

Bond pair	Interatomic distance (Å)
Y–O1	2.403(2)
Ba–O2	2.770(2)
Ba–O1	2.919(5)
Ba–O3	2.66(1)
Cu–O1	1.9396(5)
Cu–O2	2.469(9)
Hg–O2*	2.057(7)
Hg–O3*	2.10(1)
Hg–O3†	2.328(9)
Hg–O3†	2.762(2)
Hg–O3†	3.136(9)

*Along the z axis. †In-plane.

distances are reported in Table 2. The short copper–apical oxygen distance and the high degree of “buckling” of the CuO_2 planes (the Cu–O1–Cu “buckling” angle is $168.8^\circ \pm 0.3^\circ$) make the copper environment in $\text{Hg}_2\text{Ba}_2\text{YCu}_2\text{O}_{8-x}$ similar to that of $\text{YBa}_2\text{Cu}_3\text{O}_{7-x}$. On the contrary, single-Hg-layer compounds have very long copper–apical oxygen distances and nearly flat CuO_2 planes.

The $x = 0.3, 0.4$, and 0.5 samples have metallic resistances and become superconducting at low temperature. The ac susceptibility (Fig. 4) and resistivity (Fig. 5) versus temperature curves show the presence of a bulk superconducting transition at 35, 40, and 45 K for the $x = 0.3, 0.4$, and 0.5 samples, respectively, the latter two samples having a smaller onset at higher temperature (~ 70 K). The superconducting phase fractions at 4 K are $\sim 18, 100$, and 47%, respectively, without demagnetization corrections. The high shielding fractions at low temperature indicate that the main transition must be attributed to the two-mercury-layer phase. For the moment, we have no satisfactory explanation for the smaller onset at 70 K for the $x = 0.4$ and 0.5 samples. The analyses of both x-ray and neutron diffraction patterns have revealed no significant amounts of known superconducting phases in the system (like $\text{HgBa}_2\text{CuO}_4$, $\text{HgBa}_2\text{CaCu}_2\text{O}_6$, $\text{HgBa}_2\text{Ca}_2\text{Cu}_3\text{O}_8$, or $\text{YBa}_2\text{Cu}_3\text{O}_{7-x}$), although some small Bragg peaks in the neutron diffraction patterns remain unaccounted for. The resistivity of all samples drops abruptly near the diamagnetic onset and reaches zero resistance around 25 and 45 K for the $x = 0.3$ and 0.4 samples, respectively.

Our work demonstrates that the rock salt-type $(\text{HgO})_2$ block can be stabilized in layered cuprates. Despite the presence of oxygen vacancies, charge balance considerations make it reasonable to think that this structural element could be used as a high-efficiency charge reservoir for compounds with a high number of CuO_2 layers.

REFERENCES

1. M. Maeda, Y. Tanaka, M. Fukutoma, T. Asano, *Jpn. J. Appl. Phys.* **27**, 209 (1988).
2. Z. Z. Sheng and A. M. Hermann, *Nature* **332**, 55 (1988).
3. ———, *ibid.*, p. 138.
4. S. N. Putilin, E. V. Antipov, O. Chmaissem, M. Marezio, *ibid.* **362**, 226 (1993).
5. A. C. Larson and R. B. von Dreele, General Structure Analysis System, University of California (1985).

1 April 1994; accepted 18 May 1994

Crystal Structure of P22 Tailspike Protein: Interdigitated Subunits in a Thermostable Trimer

Stefan Steinbacher,* Robert Seckler, Stefan Miller, Boris Steipe, Robert Huber, Peter Reinemer*

The tailspike protein (TSP) of *Salmonella typhimurium* phage P22 is a part of the apparatus by which the phage attaches to the bacterial host and hydrolyzes the O antigen. It has served as a model system for genetic and biochemical analysis of protein folding. The x-ray structure of a shortened TSP (residues 109 to 666) was determined to a 2.0 angstrom resolution. Each subunit of the homotrimer contains a large parallel β helix. The interdigitation of the polypeptide chains at the carboxyl termini is important to protimer formation in the folding pathway and to thermostability of the mature protein.

The tailspike protein of *Salmonella typhimurium* phage P22 is a homotrimeric structural protein of 666 amino acid residues, which is noncovalently bound to the neck of the virus capsid and essential for phage adsorption to the bacterial host (1). It displays endorhamnosidase enzymatic activity, hydrolyzing the α -1,3-O-glycosidic linkage between rhamnose and galactose of *Salmonella* O-antigen polysaccharide (2).

The tailspike protein has served as a model system for the folding and assembly of large, multi-subunit proteins. The folding pathway comprises several consecutive steps, such as subunit folding and the formation of a protimer, in which the chains are stably associated but not fully folded, and a rate-limiting folding reaction from the protimer to native TSP (3). The native trimer is thermostable beyond 80°C, resistant to proteases, and not dissociated by SDS. However, even late intermediates in the folding pathway are thermolabile (4), and the folding efficiency decreases strongly with increasing temperature, both in vivo (5) and in vitro (6).

Folding of the TSP has been the subject of detailed genetic analysis, yielding a number of lethal mutations (7) and two types of point mutations affecting the folding efficiency at high temperature. (i) Temperature-sensitive folding (tsf) mutations (8) reduce the folding yield and enhance aggregation (5). There are at least 60 different tsf mutations distributed over the central third

of the TSP gene (8). (ii) Global suppressor mutations of the tsf phenotype increase the folding yield at high temperature and map to only a few sites in the gene (9). We deter-

mined the x-ray crystal structure of an NH₂-terminally shortened TSP at 2.0 Å resolution (10–12).

The shortened TSP crystallized in cubic space group $P2_13$ with one monomer in the asymmetric unit. Thus, the three subunits of the homotrimer are related by threefold crystallographic symmetry. The structure was solved by multiple isomorphous replacement (MIR) techniques (Table 1) (12). The molecule is 133 Å in length and between 35 and 80 Å in diameter (Fig. 1A). Each monomer has the overall shape of a fish and is composed of six segments corresponding to the main body, the mouth, the dorsal fin, and the first, second, and third segments of the caudal fin, respectively (Fig. 1B). The secondary structure, which was analyzed with the program DSSP (13), is dominated by three parallel (A to C) and two antiparallel β sheets (D and E). In addition, the dorsal fin contains a strongly twisted antiparallel β sheet F. There are only five short α helices, α 1 to α 5. No disulfide bridges are present in the structure.

The main body of each subunit is formed by a parallel β helix, comprising 13 complete turns (residues 143 to 540), in which parallel β strands are coiled into a large right-handed helix. The β helix is collapsed

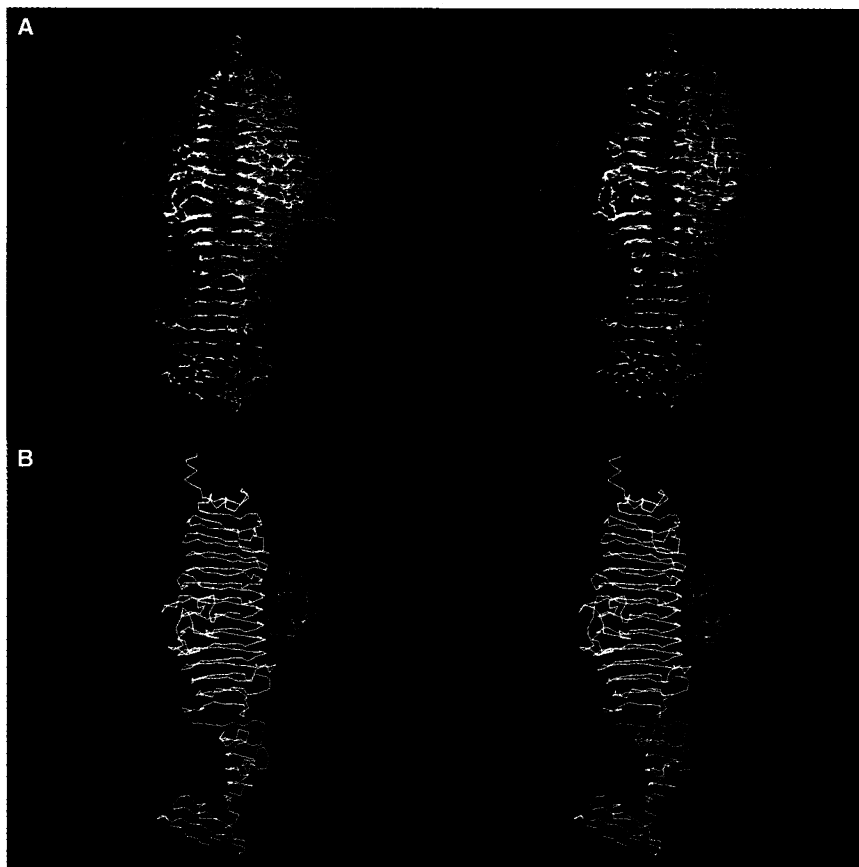


Fig. 1. Stereo view of the tertiary structure of TSP (C α traces). (A) The subunits of the trimer are shown in red, blue, and green with the NH₂-termini at the top. (B) Each subunit is composed of the mouth (yellow), the main body (orange), the dorsal fin (red), and the first (green), second (blue), and third (magenta) segments of the caudal fin.

S. Steinbacher, B. Steipe, R. Huber, P. Reinemer, Max-Planck-Institut für Biochemie, Abteilung Struktur- und Molekularbiologie, 82152 Martinsried, Germany. R. Seckler and S. Miller, Universität Regensburg, Physikalisches Institut, 93040 Regensburg, Germany.

*To whom correspondence should be addressed.